

Co-published by Institute of Fluid-Flow Machinery Polish Academy of Sciences

Committee on Thermodynamics and Combustion

Polish Academy of Sciences

Copyright@2025 by the Authors under licence CC BY-NC-ND 4.0

http://www.imp.gda.pl/archives-of-thermodynamics/



CFD based design of blast furnace gas cleaning cyclone separator

Arkadiusz Ryfa^{a*}, Mieszko Tokarski^{a,d}, Wojciech Adamczyk^a, Adam Klimanek^a, Paweł Bargiel^a, Ryszard Białecki^a, Michał Kocot^b, Marian Niesler^c, Harald Kania^c, Janusz Stecko^c, Marianna Czaplicka^c

aDepartment of Thermal Technology, Silesian University of Technology, Konarskiego 22, Gliwice 44-100, Poland
 bArcelorMittal Poland, al. Piłsudkiego 92, Dąbrowa Górnicza 41-308, Poland
 Eukasiewicz Research Network – Upper Silesian Institute of Technology, Karola Miarki 12–14, Gliwice 44-100, Poland
 dDepartment of Fuels Technology, AGH University of Science and Technology, Czarnowiejska 30, Kraków 30-059, Poland
 *Corresponding author email: arkadiusz.ryfa@polsl.pl

Received: 06.03.2025; revised: 06.06.2025; accepted: 29.07.2025

Abstract

The paper focuses on the design of the geometry and operational parameters of a cyclone separator. Its main objective is to identify a combination of dimensional and flow parameters that enables the efficient capture of large particles containing carbon and iron, while allowing particles rich in zinc and lead to pass through. The cyclone separator is intended to separate dust with a high content of valuable materials so that it can be reprocessed in a blast furnace. A computational fluid dynamics model, previously validated against similar datasets, is employed to support the design process. Three different geometries and inlet velocities ranging from 2 m/s to 12 m/s were tested to determine the most effective configuration. Depending on the selected parameters, the overall separation efficiency varied between 46% and 93%. Specifically, the system achieved separation efficiencies of 60–95% for carbon, 38–90% for iron, and 14–67% for zinc. The final design reached an overall efficiency of 86.5%, successfully separating over 90% of carbon, more than 80% of iron, as well as 45% of zinc and 55% of lead.

Keywords: Computational fluid dynamics; Cyclone; Dust; Blast furnace; Zinc

Vol. 46(2025), No. 3, 163-174; doi: 10.24425/ather.2025.156585

Cite this manuscript as: Ryfa, A., Tokarski, M., Adamczyk, W., Klimanek, A., Bargiel, P., Białecki, R., Kocot, M., Niesler, M., Kania, H., Stecko, J., & Czaplicka, M. (2025). CFD based design of blast furnace gas cleaning cyclone separator. *Archives of Thermodynamics*, 46(3), 163–174.

1. Introduction

This study aims to determine the basic geometric parameters of a cyclone used for the preliminary purification of blast furnace (BF) gas from coarse dust fractions. This cyclone represents the first stage in the BF gas cleaning process. The blast furnace produces pig iron from iron ore, coke, and fluxes. The process involves the reduction of iron ore by carbon monoxide, which is

generated through the incomplete combustion of coke. A byproduct of BF operation is blast furnace gas, characterised by high temperature, elevated pressure, a significant concentration of carbon monoxide, and a high dust content. This dust contains substantial amounts of carbon, iron, zinc, and lead.

During gas purification, a dust containing carbon and iron, valuable components for the BF process, is returned to the furnace. However, dust containing zinc and lead, which are harmful

Nomenclature

D - diameter, m

 d_{50} – cut-off point

g – mass fraction

H – height, m

m – mass, kg

r - mass ratio

Greek symbols

 α – under-relaxation factor

η – efficiency

Subscripts and Superscripts

A, B, C- simulation variant

d – dust catcher

el – element

f - fraction
gc - cleaned gas
raw- raw dust
ws - wet scrubber

Zn - zinc

Abbreviations and Acronyms

BF - blast furnace

CFD - computational fluid dynamics

CFL - flow Courant number

CS – cyclone separator

DC - dust catcher

DPM – discrete phase model

LES - large eddy simulation

RSM - Reynolds stress model

WS - wet scrubber

to the process [1], must be separated and subjected to metallurgical treatment for the recovery of these metals. Once the dust is removed, the BF gas can be expanded in turbines and used to preheat the air supplied to the tuyeres at the base of the furnace.

The various dust fractions differ in composition: coarser and medium-sized fractions tend to be richer in organic carbon (originating from coke) and iron, while finer fractions typically contain higher concentrations of zinc and lead [2]. Therefore, the cyclone should be designed to ensure efficient separation of coarse and medium-sized particles with high separation efficiency. The fine fractions are captured in a wet scrubber and removed as sludge, which is then processed externally from the ironworks. The criterion for the separation of coarse and fine fractions (i.e., the cut-off point) is based on the concentration of zinc and lead in the separated dust.

The upgrade of an obsolete BF gas cleaning system necessitated the development of a new cyclone separator. The current setup utilised a dust catcher (DC), a sizeable chamber where dust particles were separated using gravity and inertia. Despite its usage, this approach failed to offer the necessary selectivity and separation effectiveness. The enhanced system aimed to replace the dust catcher with a cyclone separator (CS). Figure 1 illustrates the former configuration of the installation.

In industrial settings, the separation of solid particles from gas or liquid is frequently required. The selection of a specific separation technique is influenced by factors like particle size and composition, along with operational conditions such as gas temperature, velocity and pressure. A common method involves using centrifugal force to extract solid particles from a rotating fluid [3], a process executed within CSs. These separators are advantageous due to their low cost, straightforward design, and minimal upkeep needs. Moreover, cyclone separators are capable of functioning under high temperatures and pressures, and they manage a broad spectrum of flow rates [4].

Cyclone separators tend to have lower effectiveness in capturing smaller particles, particularly those of sizes smaller than a micrometre. Since CSs are designed for specific dust types, any variation in dust characteristics can greatly influence their

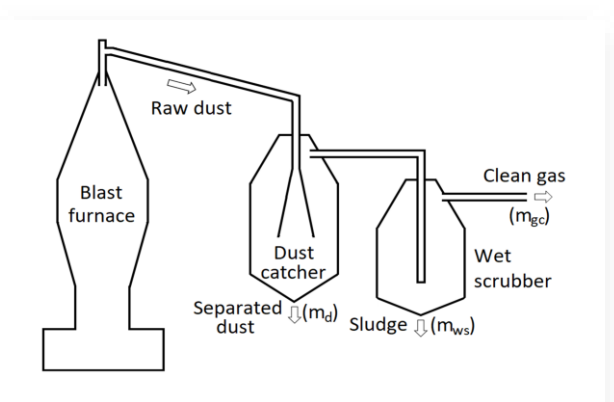


Fig. 1. Schematic of the dusting installation to be modernized with marked measurement locations.

efficiency. Cyclone efficiency is often described by the fractional efficiency curve and a cut-off point, enabling evaluation under different dust scenarios. Cyclone separators are primarily categorised into two types: axial and tangential, differentiated by their induction of swirling motion. In axial CSs, internal vanes or blades direct the gas, whereas in tangential CSs, the gas enters from one or more inlets tangentially at the top of the side wall [5]. Modifications in separation efficiency are possible for both types, with axial systems utilising adjustable vane or blade angles, and tangential systems generally employing adaptable shutters in the inlet duct. Such modifications usually necessitate a temporary halt of the system. Research on cyclones focuses on their performance and dust removal efficiency under varying conditions, using experimental and numerical methods. The effect of swirl vanes on cyclone flow is discussed in [6]. Hsu et al. [7] examined how different geometries affect cyclone efficiency, proposing a quality factor that relates to cyclone dimensions. Li et al. [8] analysed heat recovery possibilities from blast furnace slag by employing the CS. Yoshida [9] and Zhang et al. [10] studied how an apex cone influences separation efficiency. Yang et al. [11] investigated performance variations under different operational settings.

Computational fluid dynamics (CFD) is frequently employed to simulate and assess cyclone behaviour. It facilitates the examination of both established and novel cyclone designs across a variety of operational scenarios [12,13]. Such simulations typically involve optimising geometry and assessing enhancements in performance [14-17]. The potential of CFD can be augmented by incorporating deep learning techniques [18] or artificial neural networks [19], and optimisation algorithms can identify optimal operational conditions or designs. Furthermore, CFD is highly effective in determining the cut-off point for cyclone separators [3,20]. The choice of an appropriate turbulence model is crucial for precise Reynolds-averaged simulations. While simpler models like k- ε or k- ω have traditionally been used, there is a shift towards utilising the more sophisticated Reynolds stress model (RSM) [3,19-22]. The RSM turbulence model was validated for a variety of cases against experimental results and is relatively resourceefficient. An alternative technique for simulating turbulence in cyclone separators is the large eddy simulation (LES), which, although demands considerably more computational resources and a finer numerical grid, is particularly effective for studying transient turbulence fluctuations [23-25]. Cyclone separators typically operate under quasi-steady state conditions. For this reason, numerical simulations are usually performed in the steady state [26,3,27]. This approach is acceptable as long as the study aims to determine the cut-off point or the separation efficiency. Transient simulations are performed when the LES approach is used [28] or when quasi-steady flow fields are obtained by time averaging of the obtained transient fields in time [15]. Numerous papers dealing with CFD simulation of CSs, most focus on analysing a single aspect or feature of CSs. It can be a geometrical feature like apex cone [9], entrance design [22], etc., or a physical phenomenon like particle motion [25]. Furthermore, the analyses often use assumed dust parameters (size, composition, etc.). There is no complete analysis of a CS working under real conditions with the dust collected at an existing facility. Therefore, this research focuses on a robust steady-state numerical model incorporating the RSM turbulence model that is employed to determine the geometric setup and flow parameters of a full-scale industrial cyclone separator that efficiently separates valuable particles from BF gas. Dust and sludge samples were collected from the blast

furnace plant and used for comparison with the calculation results to ensure the accuracy of the obtained results.

This article is an extension of our previous study [20], in which a CFD model for a laboratory-scale axial cyclone was developed. The current work uses this model to simulate a full-scale industrial cyclone separator (CS) and tackle issues related to its dimensions and flow parameters. The primary objective is to configure the CS to effectively separate valuable materials such as iron and carbon while allowing zinc and lead, which are detrimental to the production of pig iron, to pass through [1]. Since carbon and iron are typically found in larger or denser dust particles, separating them helps conserve the natural resources and energy used in the blast furnace (BF). These larger particles generally contain minimal lead and zinc, mostly found in smaller and lighter particles. Particles not captured by the CS are removed in the second cleaning stage, often involving a wet scrubber. Another important aspect is the control of the cyclone separator, particularly due to variations in the ore composition entering the BF, which can change the dust composition. Here, the CFD model is crucial as it can forecast the cut-off point of CS.

2. Dust analysis

To design a CS, it is necessary to use the actual dust composition of the BF gas as input data. This task is complex due to the duct of the BF outlet gas configuration, high pressure, toxic carbon monoxide levels, and the duct's substantial size. To circumvent these challenges, the dust composition at the inlet was deduced from results obtained at two outputs of the existing dust removal system: DC and the wet scrubber (WS) (see Fig. 1). By gathering and examining the dust separated by the former and the sludge produced by the latter, the original dust composition was determined. At the BF plant, dust was weighed and categorised using laser diffraction according to the ISO 13320:2009 standard with the Fritsch Analysette 22 particle sizer, into size ranges between 56 µm and 1.6 mm. Smaller fractions, specifically those under 56 μm, were further divided using a counter-flow Bahco high-speed centrifuge. A total of 18 fractions were identified, with the smallest having a diameter of less than 1.9 µm. Essential elements of the dust, such as iron, carbon, zinc and lead, were determined and analysed. The dust density was measured using a pycnometer.

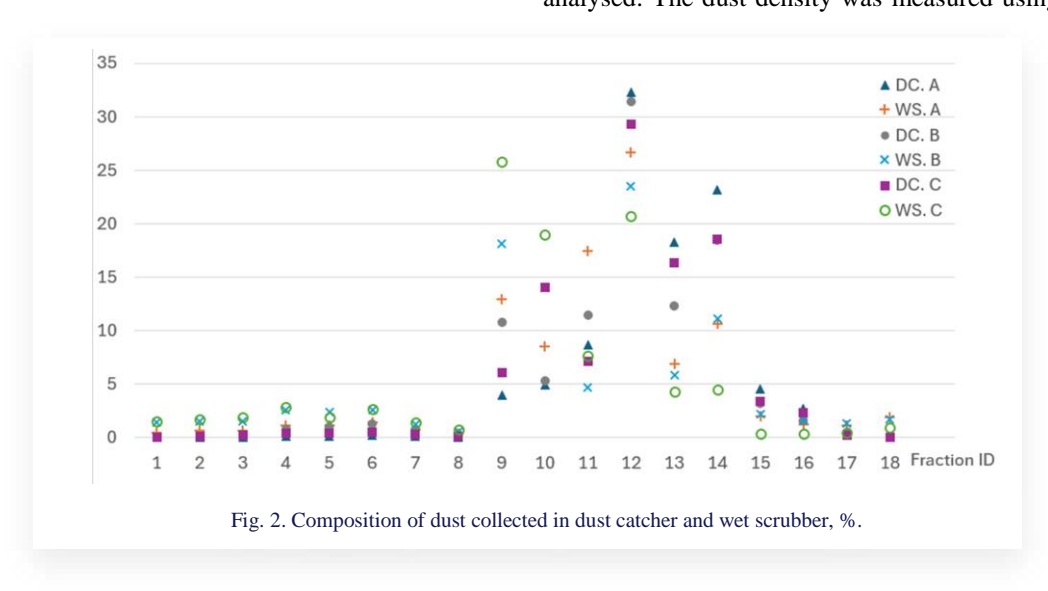


Figure 2 illustrates the detailed composition of the dust, showing three dust samples collected from DC and WS. While some variation in the dust composition is apparent, the bulk of the mass in all samples is found in medium-sized fractions, with both the smallest and largest fractions containing less than 22% of the total mass.

These measurements, combined with the known overall separation efficiency of the dust catcher ($\eta_d = 31\%$), allow to calculate the raw dust composition, that is, the dust that enters the dust removal installation. The overall separation efficiency of the dust catcher is given by

$$\eta_d = \frac{m_d}{m_{raw}},\tag{1}$$

where m_d is the mass of dust collected in the dust catcher and m_{raw} is the mass of raw dust. The same can be written separately for each fraction to obtain the fractional efficiency:

$$\eta_{d,f} = \frac{m_{d,f}}{m_{raw,f}},\tag{2}$$

where $m_{d,f}$ is the mass of fraction f of dust collected in the dust catcher, and $m_{raw,f}$ is the mass of fraction f of raw dust. The fractional efficiencies of the dust catcher are not known. The fractional mass balance can be written as

$$m_{raw,f} = m_{d,f} + m_{ws,f} + m_{gc,f},$$
 (3)

where $m_{ws,f}$ and $m_{gc,f}$ is the mass of dust separated in the wet scrubber and the mass of dust that remained in clean gas, respectively. Since the dust content after the wet scrubber $m_{gc,f}$ is approximately 1000 times less than the raw dust, it is omitted in the subsequent calculations. To find the composition of raw dust and dust catcher fractional efficiencies, a set of equations was solved:

$$\begin{cases} \sum_{f=0}^{18} g_{raw,f} = 1, \\ \eta_d = \sum_{f=0}^{18} \eta_{d,f} g_{raw,f}, \\ m_{d,f} = \eta_{d,f} m_{raw,f} & \text{for } f = 1, \dots 18, \\ m_{ws,f} = (1 - \eta_{d,f}) m_{raw,f} & \text{for } f = 1, \dots 18, \end{cases}$$

$$(4)$$

where $g_{raw,f}$ represents the mass fraction of the component f in the raw dust. This set features four primary equations. The first equation ensures that the sum of all mass fractions in the raw dust equals one. The second equation pertains to the overall efficiency of the dust collection system. The third equation details the fractional mass captured by the dust collector, derived from the second equation. The fourth equation calculates the fractional mass accumulated in the scrubber, based on the third equation. Altogether, the set includes 38 equations and 36 variables. The nonlinear gradient method was employed to solve this system. The goal was to minimise the sum of the squared residuals from the equations.

For each measurement, an independent calculation of the raw dust composition was performed and the results were presented in Fig. 3. The dust composition measurements were conducted over a three-month period. During this timeframe, both the blast furnace's operation and the iron ore's composition were considered constant. As depicted in Fig. 3, most of the dust is found in medium-sized fractions, with approximately 25% of it accumulating in the 100–160 µm range. For the simulations, the mean of the three measured compositions was utilised, and the same methodology was applied to the chemical compound content. These findings are detailed in Table 1. The measurements indicate that the bulk of the dust mass concentrates in particles sized between 71 µm and 200 µm. A mere 15% of the mass is attributed to the smallest and largest particles. Zinc, iron, and lead concentrations in the dust were analysed using an ICP-OES Agilent 5100 SVDV spectrometer. Irrespective of the fraction size, the iron content ranges from 10% to 30%, but a slight decrease is noted as particle size increases. Due to the measurement method, which involves burning the sample at 1000 K and analysing carbon dioxide in flue gas, determining organic carbon content for each fraction is unfeasible due to insufficient sample mass. Carbon content exceeds 50% in larger fractions, but is approximately 30% in smaller ones. The zinc mass fraction peaks in the smallest particles, diminishing as particle size grows. Overall, each gram of dust contains about 0.01 g of zinc, with over 70% of the zinc mass being associated with particles smaller than 71 µm. As seen in Table 1, zinc was present mainly

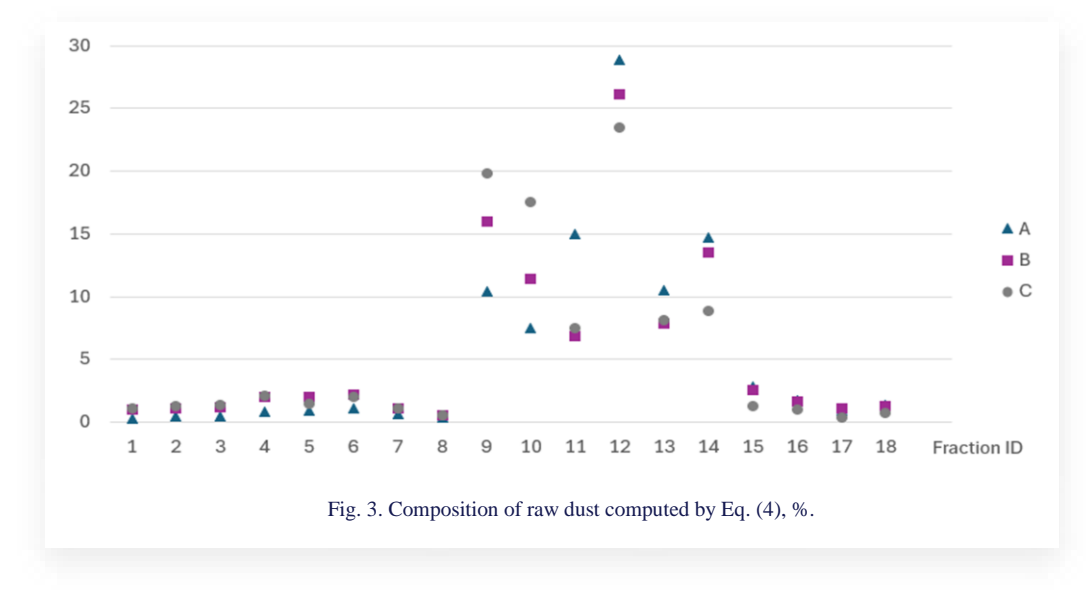


Table 1. Raw dust fractional composition and elements content.

| Frac- tion ID | Fraction, μm | Mass,% | Iron, % | Carbon,% | Zinc, % | Lead, % | |
|---------------------|-----------------|--------|---------|----------|---------|---------|--|
| 1 | <1.9 | 0.797 | 27.2 | * | 7.113 | 0.1496 | |
| 2 | 1.9-3.9 | 0.951 | 24.4 | * | 5.443 | 0.2500 | |
| 3 | 3.9-6.4 | 1.015 | 16.4 | * | 3.387 | 0.1644 | |
| 4 | 6.4-8.8 | 1.664 | 14.6 | * | 2.913 | 0.0586 | |
| 5 | 8.8-12.4 | 1.446 | 14.6 | * | 1.716 | 0.1001 | |
| 6 | 12.4-18.0 | 1.777 | * | 49.2 | 1.833 | 0.0681 | |
| 7 | 18.0-23.2 | 0.946 | 21.1 | * | 1.614 | 0.2484 | |
| 8 | 23.2-27.7 | 0.479 | 17.9 | * | 1.449 | 0.0594 | |
| 9 | 27.7-56.0 | 15.385 | 32.4 | 15.2 | 1.298 | 0.0903 | |
| 10 | 56.0-71 | 12.162 | 24.5 | 35.5 | 0.768 | 0.0455 | |
| 11 | 71–100 | 9.771 | 24.6 | 31.6 | 0.492 | 0.0520 | |
| 12 | 100-160 | 26.129 | 16.2 | 48.0 | 0.420 | 0.0787 | |
| 13 | 160-200 | 8.835 | 8.1 | 64.0 | 0.305 | 0.0765 | |
| 14 | 200-315 | 12.361 | 8.2 | 62.2 | 0.270 | 0.0860 | |
| 15 | 315-400 | 2.238 | 11.9 | 51.2 | 0.241 | 0.1415 | |
| 16 | 400-630 | 1.458 | 6.6 | 61.0 | 0.241 | 0.0659 | |
| 17 | 630-800 | 0.785 | 19.6 | 30.0 | 0.340 | 0.0639 | |
| 18 | 800-1600 | 1.118 | 20.3 | * | 0.390 | 0.0584 | |

^{*}denotes sample too small to analyse.

in the smallest fractions, with its mass fraction almost 7% for the smallest particles. With the increasing particle diameter, the zinc mass fraction shrank to less than 0.5%. The lead content does not vary with the diameter, and the overall lead content is an order of magnitude lower than that of zinc.

The dust contains a total lead content of 0.8 mg/g. A significant portion of this lead (65%) is found in medium-sized dust fractions in the diameter interval of 56–315 μ m. The primary objective of the cyclone separator is to filter out larger particles rich in iron and carbon. These particles are then recycled back

into the BF. It is crucial to minimise the quantities of zinc and lead returning to the BF due to their detrimental effects on the BF process, with zinc posing a greater risk as its amount in the dust is ten times larger than lead. The operational parameters of BF are given in Table 2. During BF work, the operating parameters may vary by approximately 20%. The dust content may also vary in terms of the fractional and zinc content. Therefore, the fractional separation efficiency of the CS needs to be evaluated.

Table 2. Measured operating parameters of blast furnace gas duct.

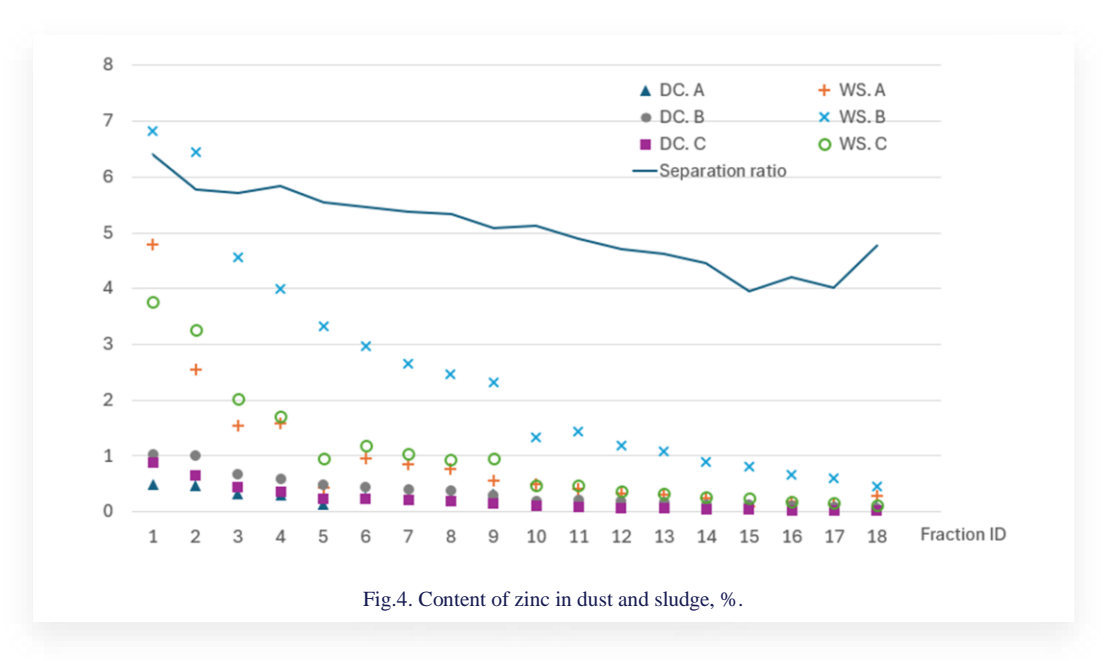
| Parameter | Value | Unit |
|----------------------|---------|-------|
| Volumetric flow rate | 396-756 | Nm³/h |
| Temperature | 243 | °C |
| Gauge pressure | 155 | kPa |
| Dust content | 15.2 | g/Nm³ |

The examination of the gathered dust and sludge (refer to Fig. 4) indicates that the sludge contains significantly higher zinc levels compared to the dust. This occurs because zinc-containing particles are lighter and, despite being larger, they tend to traverse the DC or CS due to their inertia. Conversely, smaller particles that encompass carbon and iron are denser, thus more likely to be separated than particles of the same size that contain zinc or lead. The evaluation of experimental results (refer to Figs. 2 and 4) reveals that the separation ratio of zinc in the sludge (WS) and dust (DC), as computed by the formula:

$$r_{f,Zn} = \frac{g_{Zn,ws,f}}{g_{Zn,dc,f}},\tag{5}$$

ranges from 4 to 6.

The ratio of size is typically greater for smaller and mediumsized particles, while it tends to decrease for those that are larger. This ratio helps to estimate the amount of zinc recirculated back to the BF when collecting the dust. Based on these analyses and on the chemistry of the BF process, it was determined to separate approximately 85% of the dust mass with the cyclone separator.



It is presumed that in the CS, all larger particle fractions are eliminated, whereas the smaller ones pass through, resulting in about 40% of zinc returning to the BF. In real-world operations, the separation efficiency for the largest fractions reaches 100%, albeit it is never zero for the smallest fractions. Hence, the actual amount of zinc going back to the BF is slightly higher. The separation ratio for other elements analysed was calculated as an average across all fractions employing a similar approach:

$$r_{el} = \frac{g_{el,ws}}{g_{el,dc}},\tag{6}$$

where el denotes a specific element. For instance, the separation ratios for iron, carbon, and lead are 1.4, 0.49, and 5.2, respectively.

Notably, lead demonstrates behaviour quite similar to zinc. Iron is almost evenly distributed between the dust and the sludge, whereas the amount of carbon in the dust is double that found in the sludge. These ratios will be used to assess the resources and energy savings resulting from the return of dust to the BF.

3. CFD model outline and modelling strategy

The CFD model for the CS was developed using Ansys/Fluent 19.2 and largely corresponds to the setup of a previously verified model of a lab-scale device, fully detailed in our earlier study [20]. For clarity, this text will briefly outline the parameters both models share. Conducted under steady-state conditions, the analysis yielded results akin to transient calculations but at a much lower computational expense. For 3D turbulence modelling, we employed an RSM with linear pressure strain and standard model constants, suitable for cyclonic applications. The coupled scheme was utilised for pressure-velocity coupling, while the PRESTO! scheme was applied for pressure discretisation. Convective terms of Reynolds stresses, momentum, turbulent kinetic dissipation rate, and energy were spatially discretised using the QUICK scheme. Convergence was deemed satisfactory when all residuals levelled off at 10⁻⁴ for continuity and 10⁻⁵ for velocity and turbulence. Additionally, changes in outlet velocity and pressure were monitored as further convergence indicators. To track the particles in the gas, the discrete phase model (DPM) was implemented. Reflection coefficients for the discrete phase were taken from [20], considering the particulate matter is identical in both instances and experimentally verified, with coefficients at 0.7 and 0.8 for tangential and normal components, respectively.

3.1. Geometry of the cyclone

The geometrical model of the CS consists of various elements contained in the main body, presented in Fig. 5. The particle-laden gas (1) is introduced axially at the top of the cyclone via the 3.2 m in diameter inlet and then flows around the inlet cone (6). The cone distributes the gas on the flow guides equipped with vanes (7), causing the flow to swirl (2) and thus initiating particle separation. Dust particles (4) descend due to gravity and are trapped upon reaching the inlet of the dust bin (surface 10). As the gas travels down the barrel of the cyclone, it encounters

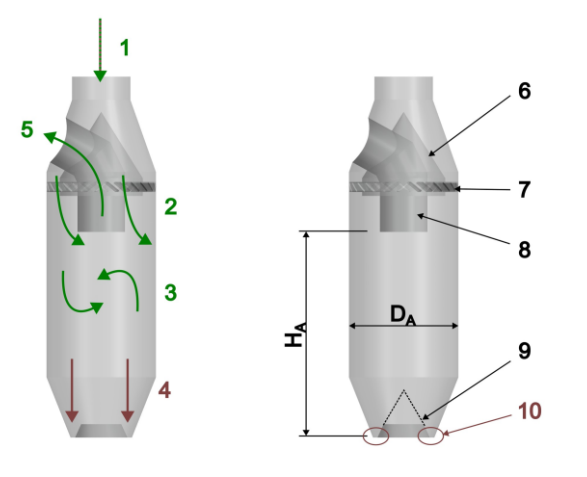


Fig.5. Cyclone – basic geometry (case A): 1 – dust-laden air inlet, 2 – air swirled by vanes, 3 – dust separation process in the cylindrical section, 4 – separated dust, 5 – purified gas outflow, 6 – inlet cone, 7 – flow guide with vanes, 8 – vortex finder, 9 – vortex cone, 10 – particle trap; D_A – cyclone internal diameter, 6 m; H_A – separation section height, 11.5 m.

a 3.37 m high conically narrowing section with a centrally located truncated vortex cone (9). This cone serves to stabilise the flow pattern within the cyclone separator. The narrowing of the barrel causes the flow to constrict, facilitating mass transfer from the outer downward vortex to the inner upward vortex. This mechanism directs the purified gas to the vortex finder (8), which eventually leaves the apparatus via the outflow pipe (5), which is 2.6 m in diameter. The vortex cone (9) is truncated, as this design choice minimally affects the velocity field while reducing the mesh size, improving its quality, and enhancing the convergence of simulations.

The main goal of this work was to numerically investigate the impact of different ratios of separation section height to barrel diameter (H/D) on the fractional separation efficiency of the axial cyclone. Hence, three cases (geometries) were considered, all presented in Fig. 6. Case A represents the baseline geometry of the height of 11.5 m in the separation section (H_A) and 6 m in the diameter of the barrel (D_A) , resulting in a H/D ratio equal to approximately 1.92. The alternative scenarios, namely B and C,

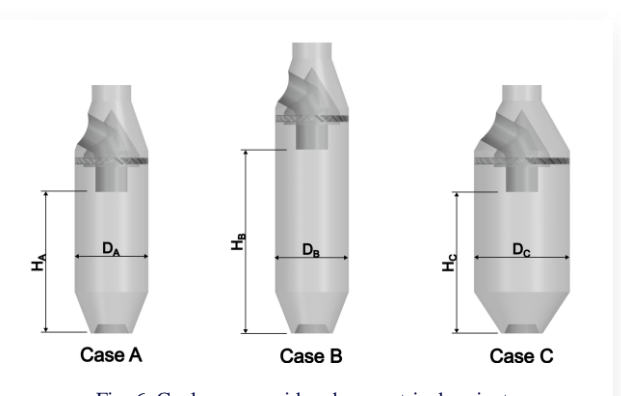
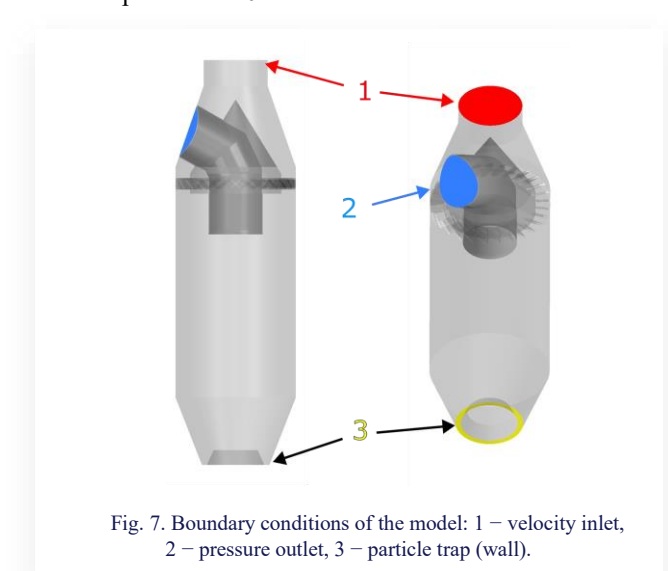


Fig. 6. Cyclone - considered geometrical variants: Case A – basic geometry, Case B – extended separation section H_B , Case C – increased diameter D_C ; $H_A = 11.5$ m, $D_A = 6$ m, $H_B = 14.95$ m, $D_B = 6$ m, $H_C = 11.5$ m, $D_C = 7.8$ m.

demonstrate modifications of the reference case, where the separation section height (H_B) was enhanced by 30%, changing from 11.5 m to 14.95 m (Case B), or the barrel diameter (D_C) was augmented from 6 m to 7.8 m (Case C). In Case B, the H/D ratio is 2.42, whereas in Case C, it stands at 1.47.

3.2. Boundary conditions

Figure 7 illustrates the three primary boundary conditions in the computational domain: (1) velocity inlet, (2) pressure outlet, and (3) particle trap (wall). Inlet (1) features a uniform velocity profile and particles evenly distributed in space. Each dust fraction is modelled as a distinct DPM injection. At the pressure outlet (2), 0 Pa gauge pressure was assumed, and the wall condition (3) acts as a particle trap. The gas used in the model is the BF gas, which is treated as an ideal gas. The heat capacity was averaged over the composition, dynamic viscosity was computed using the Wilke equation, and thermal conductivity was calculated using the Chapman-Enskog model. The composition of BF gas (see Table 3) was measured by the industrial partner. The analyses were not isothermal, so the physical properties of the BF gas were temperature-dependent, and a convective boundary condition was applied to the external walls of the cyclone, assuming a heat transfer coefficient of 16 W/(m² K) and a free stream temperature of 0 °C.

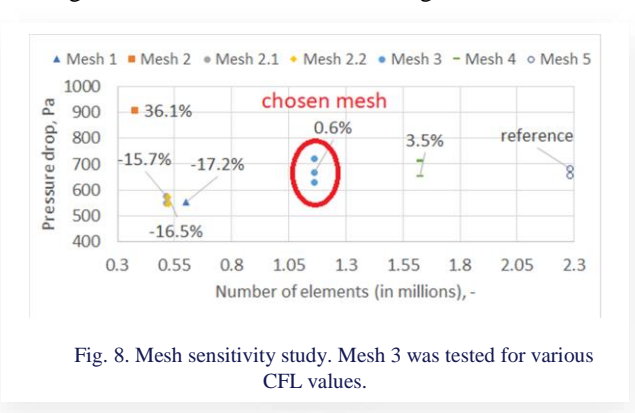


The temperature of the BF gas was 150 °C and an operating pressure was set at 2 bar. However, due to the very low temperature drop (magnitude of several °C only), the changes in the BF gas properties were insignificant. Hence, only the average values of specific heat (1085.8 J/(kg K)), thermal conductivity (0.038 W/(m K)) and dynamic viscosity (2.14×10⁻⁵ kg/(m s)) are provided here.

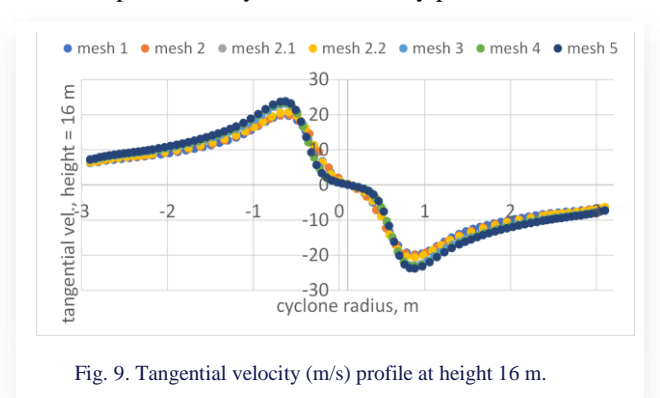
3.3. Numerical mesh

Because the pressure drop in the cyclone, defined as the difference between the static pressure at the inlet and outlet, was a significant factor for evaluating the function of the designed apparatus, it was meticulously tracked during the mesh sensitivity analysis. This study included five mesh sizes, varying from

0.37 to slightly over 2.25 million elements. As indicated in Fig. 8, where the pressure drop computed for each mesh is diplayed, increasing the number of elements to approximately 1.2 million exerts a minimal impact on the pressure drop value, as it stabilises at around 670 Pa. Relative pressure difference concerning mesh 5 is shown as labels in Fig. 8.



The same behaviour of results for various meshes can be observed on the profiles of tangential velocities across the cyclone separator (see Fig. 9). Smaller meshes (mesh 1–2.2) underpredict maximum and minimum gas velocities and do not properly resolve the stagnation at the CS axis. On the contrary, meshes 3–5 produce very similar velocity profiles.



The final mesh used in further research is presented in Fig. 10. It consists of 1.16 million mostly well-structured hexahedral elements. The only exception is the region of the inlet cone, where polyhedral elements are used instead. As previously discussed, reducing the size of the vortex cone significantly enhanced the mesh quality at the cyclone's base. Additionally, improving the mesh structure could be achieved by splitting the

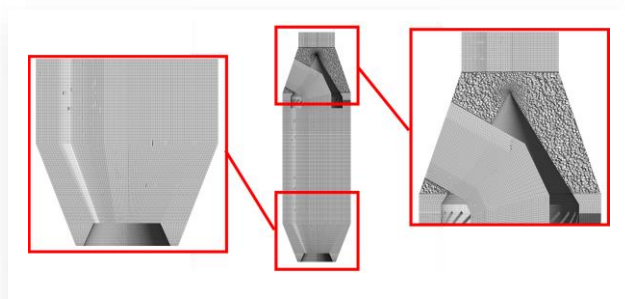


Fig. 10. Numerical mesh: 1.16 milion elements, max. skewness of 0.2, min. orthogonal quality of 0.19.

computational domain into bodies of rotational symmetry, such as the vortex finder and the area near the cyclone's axis.

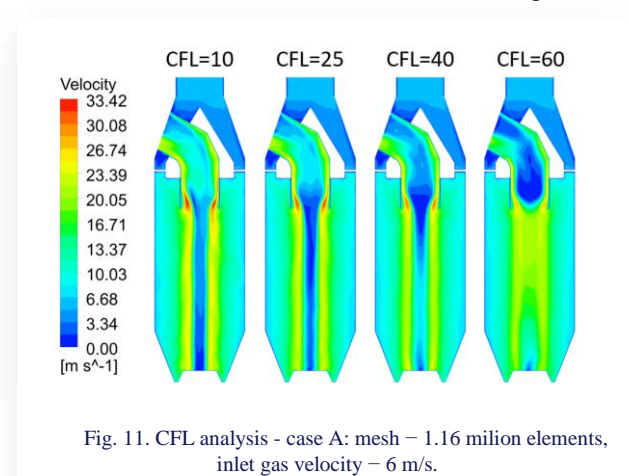
A maximum skewness of 0.25 and a minimum orthogonal quality of 0.19 ensure adequate stability and convergence for the solution. The computations were carried out on Intel(R) Core(TM) i7-5820K CPU @ 3.30GHz and 16,0 GB RAM. Solving a single case using mesh 3 took approximately 13 hours.

3.4. Courant flow number

Given the utilisation of the coupled scheme for pressure-velocity coupling, it became essential to modify the flow Courant number (CFL). This dimensionless metric indicates the number of mesh cells traversed over a specific time increment. In the context of steady-state conditions and the coupled pressure-velocity method, the CFL acts to stabilise the convergence process. The CFL is characterised as

$$CFL = \frac{\alpha}{1-\alpha},\tag{7}$$

where α represents the under-relaxation factor. Four CFL values were examined: 10, 25, 40, and 60. To select an appropriate CFL value, the velocity distribution was investigated for each scenario. Each case shared the same setup, incorporating a uniform velocity profile at the inlet, with the only variable being the distinct CFL values. The asymmetry arises from the curved outlet duct, which extends from the vortex finder, resulting in an unbalanced velocity profile with a low-velocity zone along the vertical axis. The velocity fields for each case are illustrated in Fig. 11. Notable differences in velocity distributions are evident at first glance, especially when comparing CFL = 60 and the other cases, where the low-velocity region (< 6 m/s) near the axis is heavily blurred. In the CFL = 40 scenario, the region in question is noticeable but heavily blurred in the bottom-to-centre sector. In contrast, scenarios with CFL = 10 and CFL = 25reveal a clearly defined narrow, deep blue band, indicating velocities below 6 m/s, surrounded by a high-velocity yellow/orange zone ranging from 23 to 33 m/s, with the peak velocity at the vortex finder entry. Across all profiles, there is a consistent velocity area near the walls within the separation sections (barrel and bottom cone), showing velocities between 6 and 13 m/s. The results for the CFL = 10 and CFL = 25 cases were quite similar;



however, some instabilities, observed as wavy yellow/orange regions, appeared in the CFL = 10 scenario, while the flow structure for the CFL = 25 case was more stable. Thus, CFL = 25 was chosen for further analysis.

3.5. Discrete phase model setup

The dispersion of particulate matter was simulated using the DPM, where the paths of particles were traced with a maximum of 50 000 steps and a step length factor of 5. The particle momentum exchange was accounted for by the spherical drag law combined with a discrete random walk model that included 5 iterations and a time-scale constant set at 0.15. Since the particle concentration was low, specifically 15.2 g/Nm³ interactions between particles were disregarded, and a one-way interaction between gas and particles was used. The dust was divided into 18 distinct injections, each corresponding to a specific fraction. Each injection was characterised by a constant particle diameter matching the maximum grain size of that fraction (e.g. for the 56 μm fraction, the diameter was set to 56 μm). These particles were non-reactive, with the density determined by earlier measurements. The wall reflection coefficients, based on the validation outlined in our prior research [20], were assumed to be 0.7 for tangent components and 0.8 for normal components. The dust density was assumed to be 2310 kg/m³. This value is based on measurements and is the average of all fractions.

4. Results and discussion

Once the appropriate CFL value was identified, numerical simulations were performed. The results are compiled for the three scenarios outlined earlier in Section 4.1, denoted as A, B, and C, which represent diverse geometric configurations of the cyclone. Case A serves as the reference geometry, while Cases B and C embody modifications featuring a 30% augmentation in the height of the separation section and the barrel diameter, respectively. For each configuration, the impact of gas velocity on fractional separation efficiency was examined, resulting in ten different cases with variant geometries and flow environments. In CS, higher gas velocities are desired as they enhance separation efficiencies. Consequently, Case A was tested with five distinct inlet gas velocities: 2, 4, 6, 9, and 12 m/s, to assess its influence on the flow conditions within the apparatus. The observed velocity fields are depicted in Fig. 12. The region exhibiting low velocity near the

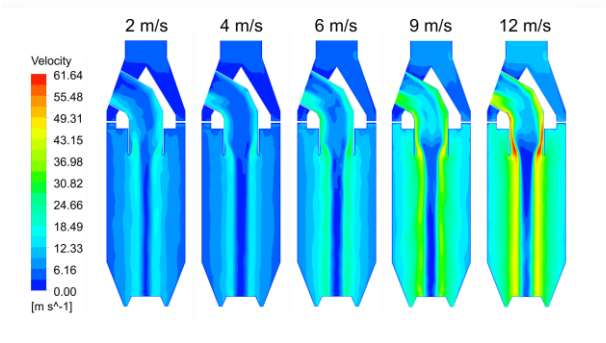
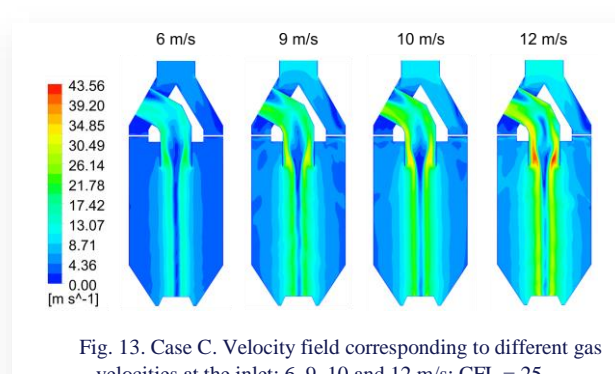


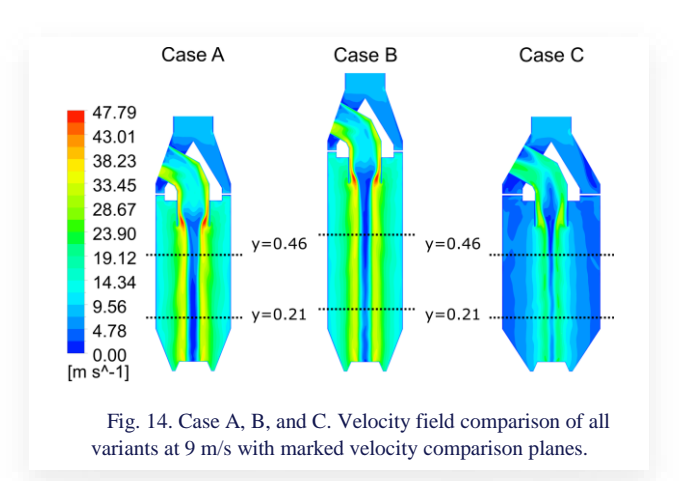
Fig.12. Case A. Velocity field in regard to different gas velocities at the inlet: 2, 4, 6, 9 and 12 m/s; CFL = 25.

central axis remains consistent and visibly apparent across all scenarios. Similarly, regions exhibiting medium to high velocity maintain stability, with no notable anomalies in flow. An increase in gas velocity substantially impacts the peak velocity at the vortex finder entrance, reaching over 60 m/s when the inlet gas velocity is set at 12 m/s. Such high velocity levels could result in excessive local erosion or vibrations. This consideration is relevant for the 9 m/s scenario, where the local velocity surpasses 40 m/s. The velocity fields recorded in case C, which features an expanded barrel diameter, are shown in Fig. 13 for four different inlet gas velocity values: 6, 9, 10, and 12 m/s. The low-velocity region along the central axis is observed, albeit smaller compared to the 6 m/s scenario. The local maximum velocity is located at the vortex finder entrance, reaching nearly 44 m/s for an inlet gas velocity of 12 m/s. This represents almost a 30% reduction compared to the related case A, also with a 12 m/s inlet gas velocity. Generally, as expected, extending the barrel diameter lowers the velocity within the cyclone globally, including the local peak velocity at the vortex finder.

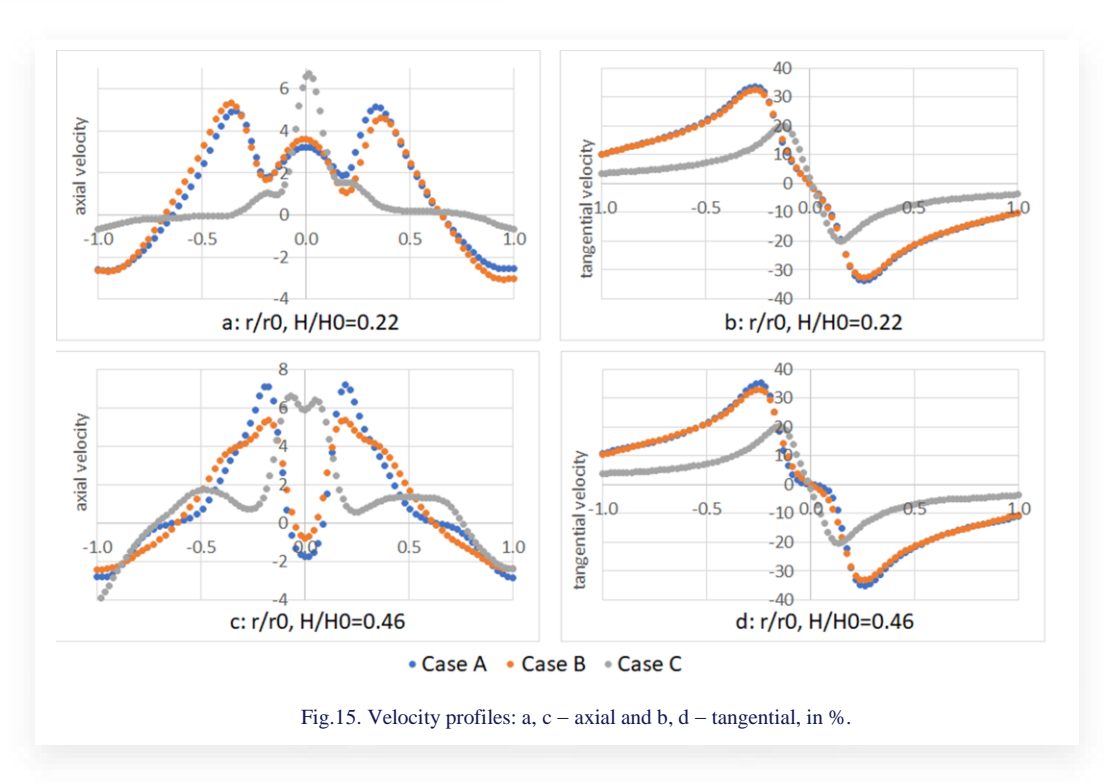
Figure 14 illustrates the velocity fields determined for a 9 m/s inlet gas velocity in the three geometric configurations examined.



velocities at the inlet: 6, 9, 10 and 12 m/s; CFL = 25.



The findings indicate that altering the height of the separation section does not influence the velocity field, as observed in similar profiles of case B (with increased height) and case A (the baseline). In both instances, the local peak velocity is around 48 m/s. However, case C (increased barrel diameter) differs, showing a reduced overall velocity with a peak of approximately 34 m/s. In Fig. 15, axial and tangential velocity profiles for all three designs at two height levels are shown. For comparison purposes, the radial coordinate was normalised. The first height was close to the outlet and was located in 22% of the overall height of CS. The second height was closer to the middle – 46% of the overall height. This analysis reveals that while the separation section's height does not notably affect the velocity field (see Fig. 14 and Figs. 15a, b, and d), the cyclone barrel's diameter significantly influences the velocity profile; specifically, enlarging the diameter markedly lowers the peak velocity and decreases the overall velocity, particularly close to the walls. In Fig. 15c, there is a visible difference between cases A and B. This is due to the larger distance from the CS outlet – the velocity field is more uniform there. As dust particles enter the cyclone, they



flow around the inlet cone and through the flow guides towards the side walls of the barrel (separation section). If the near-wall velocity is reduced, the separation efficiency should also decrease, which results from the decrease in centrifugal force. Since for Cases A and B, tangential velocities are very similar, the separation efficiency should also be at the same level. Third analysed geometry – Case C is characterised by a lower tangential velocity both near the wall and in the CS volume, thus its separation efficiency is expected to be lower. Analysing axial velocities (Figs. 15 a and c), it is visible that Cases A and B are similar, while the profile for Case C differs. For the latter, an axial velocity is much higher in the axis, while smaller near the wall. This leads to the conclusion that increasing the CS diameter lowers the separation efficiency.

To investigate the separation behaviour in terms of geometry and inlet gas velocity, the fractional separation efficiencies are gathered in Table 4, which contains the results of all the cases analysed. The table is organised column-wise, where each column corresponds to a single inlet velocity. The columns are grouped into three categories, each corresponding to a case: A, B, or C, respectively. In the very first column on the left, dust fractions are listed. The columns are filled with separation efficiencies given in percentage, according to the fraction listed in the first left column. The bottom, green-filled cells store the complete separation of a given fraction. Orange cells represent a fraction range, where the cut-off point is expected. It is defined as a fraction, half of which is separated successfully, often denoted as d_{50} [24].

Table 4 reveals that the cut-off range tends towards lower velocities, indicating a decrease in fractional separation efficiency and a shift of the cut-off point towards larger particle sizes. In Case A, particles up to 56 μm are almost fully separated with over 90% efficiency, though efficiency drops sharply for the nearest smaller particles (highlighted in orange). The cut-off particle sizes range from 23.2 to 27.7 μm at 12 m/s and from 56.0 to 71.1 μm at 2 m/s. In Case B, both the separation efficiencies and the cut-off sizes are virtually the same as in Case A when the inlet velocity is 9 m/s. Similarly, in Case C, there is

a steady decline in separation efficiency, with the cut-off point moving to larger sizes. However, there is a global shift to larger particles in the 100–200 μm range, resulting in lower overall separation efficiency. The requirement to separate 85% of dust is achievable in the CS configuration A with an inlet velocity of 4 m/s.

The overall separation efficiency is computed as

$$\eta_d = \sum_{f=0}^{18} \eta_{CS,f} \, g_{raw,f},\tag{8}$$

while the zinc separated is given by

$$\eta_{Zn} = \frac{\sum_{f=0}^{18} \eta_{CS,f,Zn} g_{CS,f,Zn}}{m_{raw,Zn}},$$
(9)

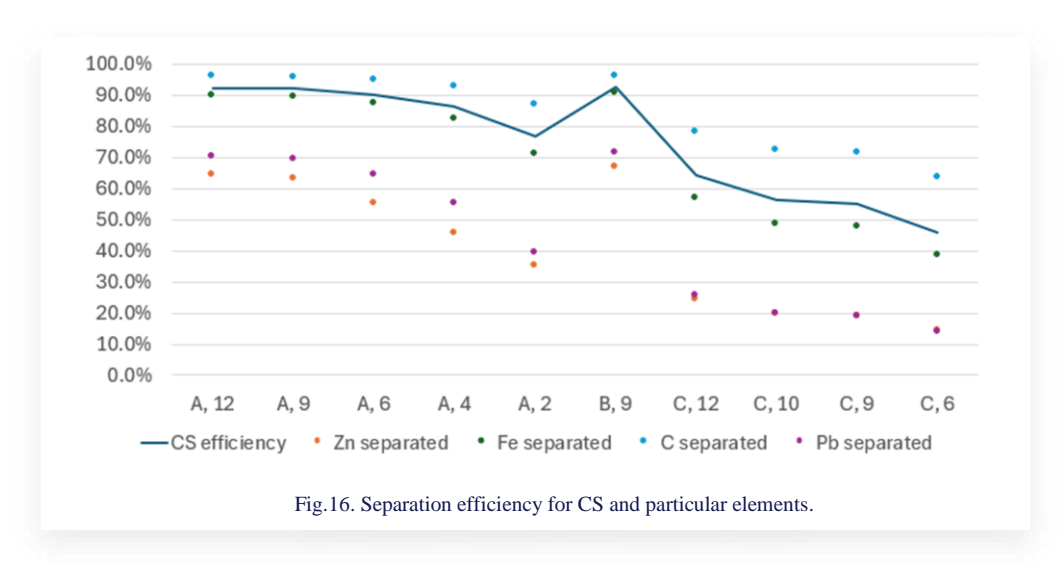
where

$$g_{CS,f,Zn} = \frac{m_{raw,f,Zn}}{\eta_{CS,f} + (1 - \eta_{CS,f})r_f},$$
(10)

where r_f is a ratio of zinc, Eq. (5), according to which it is distributed between sludge and separated dust. It is assumed that the zinc distribution between dust collected in CS and that which passes through will be the same as in DC. This cyclone separator can recover roughly 45% of the zinc (Table 4). Concurrently, about 55% of the lead is expected to return to the BF (see Fig. 16). More than 80% of iron and 90% of carbon from the dust are also anticipated to be returned to the BF. It is important to note that the volumetric flow rate of BF gas can vary significantly, potentially by $\pm 30\%$. Fluctuations in BF gas flow impact the gas velocity, thereby affecting its separation efficiency. To minimize this effect, the system includes adjustable vanes. Changing the vane angle influences the flow swirl, affecting the separation efficiency [18]. Such adjustments can, however, be made only during a pause in operations. Configuration B showcases a slightly higher efficiency at the same inlet velocity. The last geometric configuration tested exhibits a significant drop in efficiency by around 30%. Consequently, for this setup, the CS

Table 4. Fractional separation efficiency for case A, B, C at different inlet gas velocities (green – full separation; yellow expected cut-off point).

| Fraction, µm | Case A | | | | Case B | Case C | | | | |
|-----------------|--------|-------|-------|-------|--------|--------|--------|--------|-------|-------|
| | 12 m/s | 9 m/s | 6 m/s | 4 m/s | 2 m/s | 9 m/s | 12 m/s | 10 m/s | 9 m/s | 6 m/s |
| 1.9 | 15 | 3 | 9 | 8 | 7 | 13 | 7 | 6 | 5 | 7 |
| 3.9 | 20 | 9 | 12 | 9 | 11 | 25 | 9 | 6 | 8 | 7 |
| 6.4 | 24 | 19 | 17 | 15 | 8 | 27 | 10 | 5 | 11 | 7 |
| 8.8 | 25 | 25 | 26 | 27 | 7 | 30 | 10 | 5 | 7 | 7 |
| 12.4 | 28 | 34 | 31 | 31 | 17 | 35 | 10 | 4 | 13 | 8 |
| 18.0 | 35 | 39 | 37 | 38 | 21 | 35 | 20 | 5 | 10 | 8 |
| 23.2 | 47 | 45 | 41 | 38 | 29 | 43 | 21 | 7 | 12 | 7 |
| 27.7 | 52 | 51 | 45 | 38 | 36 | 49 | 22 | 7 | 12 | 9 |
| 56.0 | 97 | 96 | 88 | 68 | 41 | 99 | 31 | 16 | 17 | 18 |
| 71.1 | 100 | 100 | 96 | 90 | 55 | 100 | 36 | 23 | 24 | 23 |
| 100.0 | 100 | 100 | 100 | 100 | 100 | 100 | 44 | 37 | 34 | 30 |
| 160.0 | 100 | 100 | 100 | 100 | 100 | 100 | 87 | 78 | 72 | 44 |
| 200.0 | 100 | 100 | 100 | 100 | 100 | 100 | 100 | 98 | 99 | 84 |
| 315.0 | 100 | 100 | 100 | 100 | 100 | 100 | 100 | 100 | 100 | 100 |
| 400.0 | 100 | 100 | 100 | 100 | 100 | 100 | 100 | 100 | 100 | 100 |
| 630.0 | 100 | 100 | 100 | 100 | 100 | 100 | 100 | 100 | 100 | 100 |
| 800.0 | 100 | 100 | 100 | 100 | 100 | 100 | 100 | 100 | 100 | 100 |
| ηcs, % | 92.5 | 92.2 | 90.4 | 86.5 | 77.1 | 93.0 | 64.2 | 56.4 | 55.3 | 46.1 |
| Zn separated, % | 64.7 | 63.4 | 55.5 | 45.8 | 35.5 | 67.0 | 24.4 | 19.9 | 19.1 | 14.3 |



should keep an H/D ratio ranging from 1.5 to 2. Increasing the ratio beyond this markedly reduces efficiency and necessitates higher velocity, which is undesirable due to heightened erosion of the CS walls. In the case of Configuration A, a 20% fluctuation in gas flow alters separation efficiency by around 24% and changes zinc collection by 5%, which is an acceptable value. Considering the annual average operation parameters displayed in Table 2, the adoption of the proposed cyclone separator could conserve approximately 14 500 tons of iron and 13 000 tons of coal. This translates to a substantial conservation of natural resources and energy.

5. Conclusions

The main objective of this study was to create a comprehensive model of a cyclone separator designed to purify the blast furnace gas. This model was based on an already validated and published CFD model of a smaller-scale cyclone separator. The input to the model was derived from analysing measurements taken from a working BF gas purification system. The research was based on measurement data to determine the composition of raw dust and assess the zinc content. Using the CFD model, the influence of three factors on the separation efficiency and the amount of zinc extracted has been investigated: the inlet gas velocity, the height of the separation section and the diameter of the barrel. Gas velocity was varied between 2 and 12 m/s; two different heights for the separation section were tested: 11.5 and 14.95 m; and two barrel diameters: 6 and 7.8 meters were evaluated. Alterations in the dimensions of the cyclone separator yielded three unique geometries with different height-to-diameter ratios. A = 1.92, B = 2.42 and C = 1.47. Analysis revealed that configuration A achieved the highest dust separation efficiency (approximately 93%) at an inlet velocity of 12 m/s. Configuration B matched the dust separation efficiency of configuration A at a velocity of 9 m/s, suggesting that the separation section height minimally affects the separation efficiency. Configuration C consistently demonstrated a dust separation efficiency roughly 30% lower than A and B, at all input velocities, resulting in a reduction in zinc separation by nearly 40%. With a flow and geometric configuration of A at 4 m/s, 85% of dust and 46% of zinc are separated, resulting in minimal zinc separation (with the peak zinc separation noted at 65% for A at 12 m/s), while still achieving a notably high dust separation. This result is beneficial since the dust mainly comprises iron and carbon, which are to be recycled back into the blast furnace. The considerable quantity of dust rerouted to the BF carries only a minor amount of zinc, whose presence in the gas is detrimental to the blast furnace process.

Acknowledgements

This research was supported by the Polish Agency for Enterprise Development within grant no. POIR.01.01.01-00-099/18. One of the authors was also supported by the Ministry of Science and Higher Education, Poland, with the grant AGH UST no. 16.16.210.476 and by the NAWA Polish Returns no. 12.12.210.05020 (PPN/PPO/2019/1/00023/U/0001). Publishing was supported by the statutory research funds of the Silesian University of Technology.

References

- [1] Stanek, W., Szega, M., Blacha, L., Niesler, M., & Gawron, M. (2015). Exergo-ecological assessment of auxiliary fuel injection into blast-furnace. *Archives of Metallurgy and Materials*, 60(2), 711–719. doi: 10.1515/amm-2015-0196
- [2] Leimalm, U., Lundgren, M., Ökvist, L.S., & Björkman, B. (2010). Off-gas dust in an experimental blast furnace: Part 1: Characterization of flue dust, sludge and shaft fines. *ISIJ International*, 50(11), 1560–1569. doi: 10.2355/isijinternational.50.1560
- [3] Lim, J.-H., Oh, S.-H., Kang, S., Lee, K.-J., & Yook, S.-J. (2021). Development of cutoff size adjustable omnidirectional inlet cyclone separator. *Separation and Purification Technol*ogy, 276(12), 119397. doi: 10.1016/j.seppur. 2021.119397
- [4] Fayed, M.E., & Otten, L. (1997). Handbook of Powder Science & Technology (2nd ed.). Springer US. doi: 10.1007/9781-4615-6373-0
- [5] Hoffmann, A., & Stein, L. (2007). *Gas Cyclones and Swirl Tubes*. Springer Berlin, Heidelberg.
- [6] Celis, G.E.O., Loureiro, J.B.R., Lage, P.L.C., & Silva Freire, A.P. (2022). The effects of swirl vanes and a vortex stabilizer on the dynamic flow field in a cyclonic separator. *Chemical Engineering Science*, 248(A), 117099. doi: 10.1016/j.ces.2021.117099

- [7] Hsu, C.W., Huang, S.H., Lin, C.W., Hsiao, T.C., Lin, W.Y., & Chen, C.C. (2014). An experimental study on performance improvement of the stairmand cyclone design. *Aerosol and Air Quality Research*, 14.3, 1003–1016. doi: 10.4209/aaqr. 2013.04.0129
- [8] Li, S., Li, J., Xiao, Y., Ma, H., Chen, Y., Jiang, X., & Wang, H. (2025). Separation and recovery of waste heat from millimeter-sized blast furnace slag in cyclone separators. *Separa*tion and Purification Technology, 367, 132908. doi: 10.1016/ j.seppur.2025.132908
- [9] Yoshida, H. (2013). Effect of apex cone shape and local fluid flow control method on fine particle classification of gas-cyclone. *Chemical Engineering Science*, 85, 55–61. doi: 10.1016/j.ces.2012.01.060
- [10] Zhang, R., Yang, J., Han, S., Hao, X., & Guan, G. (2022). Improving advantages and reducing risks in increasing cyclone height via an apex cone to grasp vortex end. *Chinese Journal of Chemical Engineering*, 54, 136–143 doi: 10.1016/j.cjche.2022.04.014
- [11] Yang, X., Yang, J., Wang, S., & Zhao, Y. (2022). Effects of operational and geometrical parameters on velocity distribution and micron mineral powders classification in cyclone separators. *Powder Technology*, 407, 117609. doi: 10.1016/ j.powtec.2022.117609
- [12] Oh, J., Choi, S., & Kim, J. (2015). Numerical simulation of an internal flow field in a uniflow cyclone separator. *Powder Technology*, 274, 135–145. doi: 10.1016/j.powtec.2015.01.015
- [13] Chen, L., Ma, H., Sun, Z., Ma, G., Li, P., Li, C., & Cong, X. (2022). Effect of inlet periodic velocity on the performance of standard cyclone separators. *Powder Technology*, 402, 117347. doi: 10.1016/j.powtec.2022.117347.
- [14] Huang, A.N., Ito, K., Fukasawa, T., Yoshida, H., Kuo, H.P., & Fukui, K. (2018). Classification performance analysis of a novel cyclone with a slit on the conical part by CFD simulation. *Separation and Purification Technology*, 190, 25–32. doi: 10.1016/j.seppur.2017.08.047
- [15] Wasilewski, M., & Brar, L.S. (2019). Effect of the inlet duct angle on the performance of cyclone separators. *Separation and Purification Technology*, 213(4), 19–33. doi: 10.1016/j.seppur.2018.12.023
- [16] Zhang Y., Yang S., Hu J., Wang H. (2025). Impact of draft plate on the separation performance of gas-solid cyclone separator. *Powder Technology*, 456, 120806. doi: 10.1016/ j.powtec.2025.120806
- [17] Kumar, M., Saha, I., Pandey, S., Prakash, O., Elsayed, K., Singh Brar, L. (2025). Analysis and optimization of cyclone separators with bulged conical segments using large-eddy simulation and artificial neural network. *Separation and Purification Technology*, 370, 133247. doi: 10.1016/j.seppur. 2025.133247

- [18] Le, D.K., Guo, M., & Yoon, J.Y. (2023). A hybrid CFD Deep Learning methodology to improve the accuracy of cutoff diameter prediction in coarse-grid simulations for cyclone separators. *Journal of Aerosol Science*, 170, 106143. doi: 10.1016/j.jaerosci.2023.106143
- [19] Zhang, L., Chen, Y., Zhao, B., Dang, M., & Yao, Y. (2022). Numerical simulation on structure optimization of escapepipe of cyclone separator with downward outlet. *Powder Technol*ogy, 411, 117588. doi: 10.1016/j.powtec.2022.117588
- [20] Ryfa, A., Tokarski, M., Adamczyk, W., Klimanek, A., Bargiel, P., Białecki, R., Kocot, M., Niesler, M., Kania, H., Stecko, J., & Czaplicka, M. (2023). Determination of an axial gas cyclone separator cut-off point by CFD numerical modeling. *Archives of Thermodynamics*, 44(4), 535–562. doi: 10.24425/ather.2023.149733
- [21] Li, W., Huang, Z., Li, G., & Ye, C. (2022). Effects of different cylinder roof structures on the vortex of cyclone separators. *Separation and Purification Technology*, 296, 121370. doi: 10.1016/j.seppur.2022.121370
- [22] Wang, C.M., Wang, T.F., Fukui, K., Fukasawa, T., Hsu, W.Y., Huang, A.N., & Kuo, H.P. (2025). Novel entrance and exit designs towards fully developed dual vortexes in cyclone separators. *Advanced Powder Technology*, 36(7), 104937. doi: 10.1016/j.apt.2025.104937
- [23] Dong, S., Wang, C., Zhang, Z., Cai, Q., Dong, K., Cheng, T., & Wang, B. (2023). Numerical study of short-circuiting flow and particles in a gas cyclone. *Particuology*, 72, 81–93. doi: 10.1016/j.partic.2022.02.008
- [24] Guo, M., Yang, L., Son, H., Le, D.K., Manickam, S., Sun, X., & Yoon, J.Y. (2024). An overview of novel geometrical modifications and optimizations of gas-particle cyclone separators. *Separation and Purification Technology*, 329, 125136. doi: 10.1016/j.seppur.2023.125136
- [25] Sommerfeld, M., & Taborda, M.A. (2024). Understanding solid particle transport in a gas cyclone separator. *International Journal of Multiphase Flow*. 181, 104992. doi: 10.1016/j.ijmultiphaseflow.2024.104992
- [26] Huang, L., Yuan, J., Pan, M., Wu, J., Qiao, J., Jiang, H., & Duan, C. (2023). CFD simulation and parameter optimization of the internal flow field of a disturbed air cyclone centrifugal classifier. *Separation and Purification Technology*, 307, 122760. doi: 10.1016/j.seppur.2022.122760
- [27] Li, Y., Qin, G., Xiong, Z., & Fan, L. (2022). Gas-liquid separation performance of a micro axial flow cyclone separator. *Chemical Engineering Science*, 249, 117234. doi: 10.1016/j.ces.2021.117234
- [28] Shastri, R., Singh Brar, L., & Elsayed, K. (2022). Multi-objective optimization of cyclone separators using mathematical modelling and large-eddy simulation for a fixed total height condition. Separation and Purification Technology, 291, 120968. doi: 10.1016/j.seppur.2022.120968